

# Redshift–Space Distortions and the Real–Space Clustering of Different Galaxy Types

Luigi Guzzo<sup>1,2</sup>, Michael A. Strauss<sup>1,3</sup>, Karl B. Fisher<sup>4,5</sup>,

Riccardo Giovanelli<sup>6</sup>, and Martha P. Haynes<sup>6</sup>

## ABSTRACT

We study the distortions induced by peculiar velocities on the redshift–space correlation function of galaxies of different morphological types in the Pisces–Perseus redshift survey. Redshift–space distortions affect early– and late–type galaxies in different ways. In particular, at small separations, the dominant effect comes from virialized cluster cores, where ellipticals are the dominant population. The net result is that a meaningful comparison of the clustering strength of different morphological types can be performed only in real space, i.e., after projecting out the redshift distortions on the two–point correlation function  $\xi(r_p, \pi)$ . A power–law fit to the projected function  $w_p(r_p)$  on scales smaller than  $10 h^{-1}$  Mpc gives  $r_0 = 8.35_{-0.76}^{+0.75} h^{-1}$  Mpc,  $\gamma = 2.05_{-0.08}^{+0.10}$  for the early–type population, and  $r_0 = 5.55_{-0.45}^{+0.40} h^{-1}$  Mpc,  $\gamma = 1.73_{-0.08}^{+0.07}$  for spirals and irregulars. These values are derived for a sample luminosity limited to  $M_{Zw} \leq -19.5$ . We detect a 25% increase of  $r_0$  with luminosity for all types combined, from  $M_{Zw} = -19$  to  $-20$ . In the framework of a simple stable–clustering model for the mean streaming of pairs, we estimate  $\sigma_{12}(1)$ , the one–dimensional pairwise velocity dispersion between 0 and  $1 h^{-1}$  Mpc, to be  $865_{-165}^{+250} \text{ km s}^{-1}$  for early–type galaxies and  $345_{-65}^{+95} \text{ km s}^{-1}$  for late types. This latter value should be a fair estimate of the pairwise dispersion for “field” galaxies; it is stable with respect to the presence or absence of clusters in the sample, and is consistent with the values found for non–cluster galaxies and *IRAS* galaxies at similar separations.

*Subject headings:*

---

<sup>1</sup>Department of Astrophysical Sciences, Princeton University, Princeton, NJ 08544.

<sup>2</sup>Permanent Address: Osservatorio Astronomico di Brera, Via Bianchi 46, I–22055 Merate (LC), Italy.

<sup>3</sup>Alfred P. Sloan Foundation Fellow.

<sup>4</sup>Institute for Advanced Study, Olden Lane, Princeton, NJ 08540

<sup>5</sup>Current Address: Signal Physics Group, Applied Research Laboratories, The University of Texas, Austin, Texas, 78713

<sup>6</sup>Department of Astronomy and Center of Radiophysics and Space Research, Space Sciences Bldg., Cornell University, Ithaca, NY 14853

## 1. INTRODUCTION

Peculiar velocities distort the maps of the galaxy distribution when redshifts are used as a measure of distance through the Hubble relation. The observed distortions contain important information on the statistical properties of the large-scale motions of galaxies, presumably due to the gravitational influence of the true underlying mass distribution. In particular, the two-point correlation function in redshift space  $\xi(s)$  differs from that in real space  $\xi(r)$  in two respects: on small scales correlations are suppressed due to the virialized motions in rich clusters, which in redshift space elongate structures along the line of sight; on large scales coherent motions produced by infall into overdense regions or by outflow out of underdense regions enhance correlations.

Galaxies of different morphological types inhabit different environments, following a well-established morphology–density relation (e.g., Dressler 1980; Postman & Geller 1984). As a consequence, they display significantly different clustering properties (Davis & Geller 1976; Giovanelli, Haynes & Chincarini 1986; Iovino *et al.* 1993; Loveday *et al.* 1995; Hermit *et al.* 1996): ellipticals and S0’s dominate dense cluster cores and are therefore more clustered than spirals and irregulars. However, their association with the deep potential wells of clusters implies that they have higher peculiar velocities on average, so that the small-scale  $\xi(s)$  for early-type galaxies is more strongly suppressed with respect to  $\xi(r)$  than for late types. The consequence is that a correct comparison of the clustering properties of different morphological types requires understanding in detail their respective redshift space distortions. One way to avoid this problem is to measure the angular correlation function  $w(\theta)$  on two-dimensional catalogues (Giovanelli *et al.* 1986; Loveday *et al.* 1995<sup>7</sup>). The effects of redshift space distortions also need to be quantified in comparing the angular clustering of distant objects with the clustering in redshift space of galaxies at low redshift (e.g., Iovino *et al.* 1996).

The standard way to quantify redshift distortions is to split the separation vector of a pair of objects into components lying on the plane of the sky,  $r_p$ , and along the line of sight,  $\pi$ , and to compute the correlation function  $\xi(r_p, \pi)$  as a function of these two components. The iso-correlation contours of  $\xi(r_p, \pi)$  will be stretched along the  $\pi$  direction at small separations, due to the effect of large velocity dispersions, and compressed at large scales, as a consequence of large-scale coherent motions. Projecting  $\xi(r_p, \pi)$  onto the  $r_p$  axis gives the projected function  $w_p(r_p)$ , which is independent of redshift distortions and can be directly expressed as an integral over the real-space correlation function  $\xi(r)$ . The equation relating  $w_p(r_p)$  and  $\xi(r)$  thus allows one to recover the latter via direct inversion or modelling.

On the other hand, modelling the distortions of  $\xi(r_p, \pi)$  allows one to characterize the pairwise velocity distribution function. We are particularly concerned with the second moment of this distribution function,  $\sigma_{12}(r)$ , in this paper. Davis & Peebles (1983, hereafter DP83) used the

---

<sup>7</sup>These latter authors perform also a cross-correlation between morphological subsamples of the APM–Stromlo redshift survey and the APM angular catalogue, see § 4.2.

CfA1 survey (Huchra *et al.* 1993) to measure  $\sigma_{12}(1)$ , the value of  $\sigma_{12}(r)$  at  $r = 1 h^{-1}$  Mpc, to be  $340 \pm 40 \text{ km s}^{-1}$ . While the analysis of the *IRAS* 1.2 Jy redshift survey by Fisher *et al.* (1994b, hereafter F94b) produced a similar result,  $\sigma_{12}(1) = 317_{-49}^{+40} \text{ km s}^{-1}$ , re-analyses of the CfA1 survey (Mo, Jing & Börner 1993, Zurek *et al.* 1994, Somerville, Davis & Primack 1996), and of larger optical redshift surveys have shown a large range of values, going as high as  $1000 \text{ km s}^{-1}$  (Marzke *et al.* 1995, Guzzo *et al.* 1996, Lin 1995). In particular,  $\sigma_{12}(1)$  is found to be quite sensitive to the presence or absence of one or two rich clusters, even in volumes as large as the CfA2. It seems plausible that while the CfA1 value was strongly affected by the smallness of the volume surveyed, that measured from the *IRAS* 1.2 Jy survey reflects the specific nature of *IRAS* galaxies, which are mostly star-forming, late-type galaxies which are under-represented in rich clusters relative to optically selected galaxies (Strauss *et al.* 1992).

The case of *IRAS* galaxies explicitly illustrates the dangers of using a specific class of objects to draw conclusions on statistics of the velocity field, in particular at small separations: the answer depends sensitively on the morphological type of the tracer we are using. This paper addresses this issue in detail: 1) What is the difference in the clustering strength of early- and late-type galaxies measured in real space? 2) What is the small-scale velocity dispersion for the two classes of objects?

The outline of the paper is as follows: in § 2, we present the data we will use for our analyses. We discuss the measurement of  $\xi(r_p, \pi)$  in § 3, and present our results in § 4. Our conclusions are summarized in § 5.

## 2. THE DATA: DEFINITION OF THE SAMPLES

We use the Perseus–Pisces redshift catalogue (cf., Giovanelli & Haynes 1991), which includes redshifts for all Zwicky galaxies (Zwicky *et al.* 1961–1968) in the positive-declination part of the South Galactic Cap (i.e., about  $21^h \leq \alpha \leq 5^h$ ,  $0^\circ \leq \delta \leq 50^\circ$ ). As Giovanelli, Haynes & Chincarini 1986 make clear, the Perseus–Pisces redshift survey is affected by Galactic extinction around the edges. For statistical studies, therefore, it has to be properly restricted. The Zwicky catalogue is nominally complete to  $m_{Zw} = 15.7$ : we thus impose an extinction-corrected magnitude cut of 15.5, trim the survey to  $22^h \leq \alpha \leq 4^h$ ,  $0^\circ \leq \delta \leq 42^\circ$ , and apply the additional cut indicated by the heavy line of Figure 1. This excludes nearly all regions with absorption  $A_B > 0.2$ , as given by the extinction maps of Burstein & Heiles (1978), while it leaves in the core of the Perseus cluster ( $\alpha \sim 3.2^h$ ,  $\delta \sim +41^\circ$ ) to allow us to study the robustness of our results to the presence of the richest cluster in the region. The magnitude-limited sample selected in this way contains 4111 galaxies. One potential problem of our selection criteria is that they push the Zwicky catalogue to its completeness limit. In particular, with the extinction correction we include galaxies with observed Zwicky magnitudes  $m_{Zw} \gtrsim 15.5$ , where magnitude errors are large (e.g., Bothun & Cornell 1990). We shall show in § 4.2 that our principal results are indeed quite robust to these uncertainties in the parent photometric catalogue.

All the analyses of this paper are done with volume-limited subsamples of the data. That is, we select a lower-limiting luminosity (or equivalently, an upper limit in absolute magnitude), and a corresponding maximum distance implied by our apparent magnitude limit, giving us uniform sampling throughout the volume. This has the effect of de-emphasizing the Pisces-Perseus chain relative to the magnitude-limited case, because in the latter, the selection function peaks near the redshift of the supercluster. Also, this choice is crucial for discussing luminosity effects, and eliminates uncertainties related to the weighting schemes necessary when analysing magnitude-limited samples.

Table 1 summarizes the parameters of the volume-limited samples we have used. The range of absolute magnitudes covered by the subsamples reflects the need to maximize our volume, while keeping a sufficient number of objects within it. Absolute magnitudes were calculated assuming  $H_0 = 100 \text{ km s}^{-1} \text{ Mpc}^{-1}$ . The E-19.5 sample (“ellipticals”) contains galaxies with early morphological types (E, S0, and S0a), while the S- samples (“spirals”) contain all galaxies classified as spirals or irregulars. The morphological information available in the catalogue is in reality quite finer, subdivided into 14 classes. The morphological coding is from the UGC for those galaxies in that catalog, and has been estimated from sky survey plates for the remainder of the galaxies (Giovanelli, Haynes & Chincarini 1986). To maximize the statistics within the volume-limited samples, we restrict our analysis to the two broad groups of early- and late-type galaxies. The spiral class is however large enough to define several samples to different absolute magnitudes (S-19, S-19.5, and S-20); we also define a spiral sample trimmed to exclude the Perseus cluster (S-19.5-NOP). Finally, we define an equivalent sample including all morphologies for comparison, PP-19.5-NOP.

The cone diagrams of Figure 2 show the galaxy distribution in PP-19.5 and PP-20, in which all morphological types are included, while Figure 3 shows the corresponding distribution of the E-19.5 and S-19.5 samples, respectively. Note that the Perseus-Pisces chain, the overdensity at  $cz \approx 6000 \text{ km s}^{-1}$ , is more prominent in the ellipticals than the spirals, consistent with the observed distribution on the sky (Giovanelli, Haynes & Chincarini 1986). This is made quantitative in Figure 4, which shows the redshift histogram of each of these subsamples; the dashed line in each case, proportional to  $r^2$ , gives the expected distribution in the absence of structure.

### 3. ESTIMATING THE TWO-POINT CORRELATION FUNCTION IN REDSHIFT SPACE

#### 3.1. Definitions of $r_p$ and $\pi$

The effect of redshift-space distortions can be understood through the correlation function  $\xi(r_p, \pi)$ , where the radial separation of pairs is split into two components:  $\pi$ , parallel to the line of sight, and  $r_p$ , perpendicular to it. There are two definitions of these quantities in the literature.

Given two galaxies at redshifts  $v_1$  and  $v_2$ , separated by angle  $\theta$ , DP83 define:

$$\pi \equiv \frac{1}{H_0} |v_1 - v_2| \quad r_p \equiv \frac{1}{H_0} (v_1 + v_2) \tan \frac{\theta}{2}. \quad (1)$$

Note that the quadrature sum of  $r_p$  and  $\pi$  is *not* equal to the redshift space distance  $s$  between the galaxies. Recognizing this, Fisher *et al.* (1994a, hereafter F94a) use a slightly different definition. They define the line of sight vector  $\mathbf{l} \equiv (\mathbf{v}_1 + \mathbf{v}_2)/2$  and the redshift difference vector  $\mathbf{s} \equiv \mathbf{v}_1 - \mathbf{v}_2$ , leading to the definitions

$$\pi \equiv \frac{\mathbf{s} \cdot \mathbf{l}}{H_0 |\mathbf{l}|} \quad r_p^2 \equiv \frac{\mathbf{s} \cdot \mathbf{s}}{H_0^2} - \pi^2. \quad (2)$$

If we recast the F94a formulation in terms of  $\theta$ , we find:

$$\pi = \frac{1}{H_0} |v_1 - v_2| + \mathcal{O}(\theta^2) \quad r_p \simeq \frac{1}{H_0} (v_1 + v_2) \tan \left( \frac{\theta}{2} \right) \frac{4v_1 v_2}{(v_1 + v_2)^2}, \quad (3)$$

which shows explicitly that the two definitions are *not* strictly equivalent, even in the small-angle approximation. For our analysis we use Eq. (2), but checks using Eq. (1) show only negligible differences in our  $\xi(r_p, \pi)$  maps. We conclude therefore that one can make direct comparison of results obtained with the two different definitions.

### 3.2. Measuring $\xi(r_p, \pi)$

We estimate the quantity  $\xi(r_p, \pi)$  using the method of DP83. A catalog of  $n_R = 100,000$  uniformly distributed points with the same boundaries as the real sample is prepared. We count the number of pairs in  $1 h^{-1} \text{Mpc}$  bins of  $r_p$  and  $\pi$  among the  $n_G$  galaxies  $[N_{GG}(r_p, \pi)]$ , and between the galaxies and the random sample  $[N_{GR}(r_p, \pi)]$ . Our estimate of the correlation function is then

$$\xi(r_p, \pi) = \frac{N_{GG}(r_p, \pi) 2n_R}{N_{GR}(r_p, \pi) n_G} - 1. \quad (4)$$

Because our samples are volume-limited, each galaxy gets equal weight, and thus we do not apply the statistical weights needed when analyzing magnitude-limited catalogues. For the most part, we confine ourselves to scales less than  $10 h^{-1} \text{Mpc}$ , and thus there is little benefit to using the alternative estimator of Hamilton (1993). This is less sensitive than is Eq. (4) to uncertainties in the mean density, and therefore is important when measuring the correlation function on very large scales.

### 3.3. Error Estimation and Maximum-Likelihood Fits

Following Ling *et al.* (1986), we use bootstrap resampling to compute statistical errors on our estimates of quantities we derive from  $\xi(r_p, \pi)$ . As we will see in the next section, we carry

out quantitative analyses not on  $\xi(r_p, \pi)$  directly, but rather two derived quantities:  $w_p$  (Eq. 5, the projection of  $\xi(r_p, \pi)$  on the  $r_p$  axis, which does not suffer redshift-space distortions), and  $\xi(\pi)$  (Eq. 11, essentially a cut in  $\xi(r_p, \pi)$  at constant  $r_p$  to measure redshift space distortions). We thus compute errors, and the covariance matrix, of the 1-D quantities  $w_p$  and  $\xi(\pi)$ , rather than of the 2-D  $\xi(r_p, \pi)$ . For each of the samples of Table 1, we create 100 bootstrap realizations, and compute  $w_p$  and  $\xi(\pi)$  for each. Determination of the covariance matrix of errors is then straightforward, following F94a. F94a have discussed the method in detail, showing that it gives a good representation of true statistical errors for the correlation function on scales below  $\sim 10 h^{-1}$  Mpc, but it tends to overestimate them on larger scales.

This covariance matrix enables us to fit models for the real space correlation function  $\xi(r)$  and the redshift distortions to the observed  $w_p$  and  $\xi(\pi)$  via  $\chi^2$  (cf., F94b). In practice, the effective number of degrees of freedom in the data is smaller than the number of sampled values of  $w_p$  and  $\xi(\pi)$  (i.e., these functions are oversampled), and thus the covariance matrix is singular. We therefore follow F94b in using singular value decomposition, which allows the calculation of the matrix product in the  $\chi^2$  function in a robust manner.

## 4. REDSHIFT-SPACE DISTORTIONS: $\xi(r_p, \pi)$

### 4.1. The Observed $\xi(r_p, \pi)$

Figures 5–7 display the observed  $\xi(r_p, \pi)$  both for the complete samples PP–19, PP–19.5, PP–20, and for the morphological subsamples E–19.5 and S–19.5. For PP–19, we show the original  $\xi(r_p, \pi)$ , while for all samples, we show a version smoothed by a  $3 h^{-1}$  Mpc  $\times$   $3 h^{-1}$  Mpc Gaussian to suppress the binning noise and to bring out the global features of the maps. All the statistical analyses below are of course carried out on the unfiltered data.

The contours for PP–19 and PP–19.5 are enormously distorted at very small scales, a signature of a high pairwise dispersion  $\sigma_{12}(r)$  at small  $r$ , as we shall quantify in § 4.3. Most of this distortion is produced by pairs lying in clusters, in particular in the smallest sample, PP–19, which is dominated by half-dozen rich clusters along the Perseus–Pisces chain. The small-scale elongations are substantially smaller in the PP–20 sample. This sample has a volume of  $7.4 \times 10^5 h^{-3}$  Mpc<sup>3</sup>; this is quite a bit larger than the volume of PP–19.5, but it does not include any more clusters, and therefore the cluster contribution to  $\sigma_{12}(1)$  is somewhat diluted. This volume is still a factor of 6 smaller than the volume at which Marzke *et al.* (1995) show – using both a COBE-normalized Cold Dark Matter model and a phenomenological model based on the observed distribution of Abell cluster velocity dispersions – that  $\sigma_{12}(1)$  stabilizes. For samples of volume comparable to those used here, they derive a typical uncertainty on  $\sigma_{12}(1)$  of  $\sim 180 \text{ km s}^{-1}$ . Although this scatter refers to non-overlapping samples, it does give an explanation for the observed difference in  $\sigma$  for PP–19 and PP–20.

On large scales, the compression of  $\xi(r_p, \pi)$  for PP–19 (in particular the  $\xi(r_p, \pi) = 0.2$  and  $\xi(r_p, \pi) = 0$  contours) is that expected due to large-scale streaming (cf., F94b). However, the Perseus-Pisces supercluster (cf., Figure 2) lies largely in the plane of the sky, so that the real-space distribution of galaxies is intrinsically anisotropic in this sample. Thus it is not a fair sample for measuring large-scale streaming. Some part of the observed distortions of the  $\xi(r_p, \pi)$  contours must be due to infall onto the supercluster itself, as directly observed by Giovanelli *et al.* (1996), who showed that galaxies out to  $20 h^{-1}$  Mpc from the ridge display infall velocities of the order of  $1000 \text{ km s}^{-1}$  (see also Willick 1990; Eisenstein *et al.* 1997). Unfortunately, there is no way to disentangle the two effects from  $\xi(r_p, \pi)$  alone, and we will not discuss the large-scale distortions further in this paper.

Figure 7 shows  $\xi(r_p, \pi)$  for E–19.5 and S–19.5. The visual difference between the two maps is impressive; the ellipticals display a huge small-scale elongation of the contours, while  $\xi(r_p, \pi)$  for the spirals is much more isotropic. This figure demonstrates directly how different the dynamical behaviors of the two populations are, and how their real-space correlation functions are mapped into redshift space in very different ways.

We now go on to quantify the real space correlation function, and the redshift distortions, from the observed  $\xi(r_p, \pi)$ .

## 4.2. The Real-Space Correlation Function

We project  $\xi(r_p, \pi)$  onto the  $r_p$  axis by integrating over the dimension on which the redshift-space distortion acts, giving a quantity that is independent of the form and amount of the distortion itself,

$$w_p(r_p) \equiv 2 \int_0^\infty dy \xi(r_p, \pi) = 2 \int_0^\infty dy \xi \left[ (r_p^2 + y^2)^{1/2} \right], \quad (5)$$

where the second equality follows from the independence of the integral on the redshift-space distortions. In the expression on the right-hand side,  $\xi$  is the *real-space* correlation function, evaluated at  $r = (r_p^2 + y^2)^{1/2}$ . Modelling  $\xi(r)$  as a power law,  $\xi(r) = (r/r_0)^{-\gamma}$  allows us to carry out the integral analytically, yielding

$$w_p(r_p) = r_p \left( \frac{r_0}{r_p} \right)^\gamma \frac{\Gamma(\frac{1}{2}) \Gamma(\frac{\gamma-1}{2})}{\Gamma(\frac{\gamma}{2})} \quad (6)$$

where  $\Gamma$  is the Gamma function. We choose  $\pi_{up}$ , the upper integration limit in Eq. (5), to be large enough to give a stable estimate of  $w_p$ .

For the PP–19 sample,  $w_p(r_p)$  is quite insensitive to  $\pi_{up}$  in the range  $20 h^{-1} \text{ Mpc} < \pi_{up} < 30 h^{-1} \text{ Mpc}$  for  $r_p < 10 h^{-1} \text{ Mpc}$ . For larger values of  $r_p$ ,  $w_p(r_p)$  is in fact fairly sensitive to  $\pi_{up}$ ,

Sample	$M_{lim}$	$d_{lim} (h^{-1} \text{ Mpc})$	Morphology	$N_{gal}$
PP-19	-19	79	All	1021
PP-19.5	-19.5	100	All	852
PP-19.5-NOP	-19.5	100 (No Perseus)	All	803
PP-20	-20	126	All	577
S-19	-19	79	Late	565
S-19.5	-19.5	100	Late	481
S-19.5-NOP	-19.5	100 (No Perseus)	Late	458
S-20	-20	126	Late	333
E-19.5	-19.5	100	Early	278

Table 1: Properties of the volume-limited subsamples analyzed.

Sample	$r_0 (h^{-1} \text{ Mpc})$	$\gamma$
PP-19	$5.95^{+0.27}_{-0.31}$	$1.93^{+0.04}_{-0.07}$
PP-19.5	$6.95^{+0.37}_{-0.32}$	$1.88^{+0.05}_{-0.07}$
PP-19.5-NOP	$6.55^{+0.34}_{-0.36}$	$1.86^{+0.04}_{-0.05}$
PP-20	$7.05^{+0.47}_{-0.59}$	$1.72^{+0.09}_{-0.10}$
S-19	$4.55^{+0.36}_{-0.36}$	$1.65^{+0.06}_{-0.07}$
S-19.5	$5.55^{+0.40}_{-0.45}$	$1.73^{+0.07}_{-0.08}$
S-19.5-NOP	$5.05^{+0.54}_{-0.48}$	$1.76^{+0.08}_{-0.10}$
S-20	$5.05^{+0.61}_{-0.65}$	$1.85^{+0.08}_{-0.09}$
E-19.5	$8.35^{+0.75}_{-0.76}$	$2.05^{+0.10}_{-0.08}$

Table 2: Best-fit parameters of the real-space correlation function from  $w_p(r_p)$ .

but since we are primarily interested in the redshift distortions on small scales, this has no effect on our result.

The observed  $w_p(r_p)$  and the best-fit power law for the complete samples are shown in Figure 8, together with likelihood contours on  $r_0$  and  $\gamma$ , while the results of the fits are reported in Table 2. Note how well the power-law model fits the data<sup>8</sup>. Error bars are given by the scatter over 100 bootstrap realizations and the fit is performed as discussed in § 3.3. There is evidence of a growth of the correlation length with increasing sample depth and intrinsic luminosity. This is most significant ( $\sim 3\sigma$ ) between PP-19 and PP-19.5;  $r_0$  does not grow significantly between PP-19.5 and PP-20. This is in qualitative agreement with the results of Iovino *et al.* (1993) using a previous version of this sample, and the results of Loveday *et al.* (1995) on the APM-Stromlo redshift survey, but is in contrast with Hamilton (1988), who found that the luminosity dependence of  $r_0$  was most significant at the highest luminosities. Table 2 also shows a similar trend for the spiral-only samples. Thus even within morphological classes, a luminosity dependence of clustering does exist (Iovino *et al.* 1993; cf., their Figure 12). We have checked the sensitivity of these results to magnitude errors at the faint end by cutting the PP-19, PP-19.5 and PP-20 samples at a corrected magnitude  $m_{Zw} = 15.2$ , and re-computing  $\xi(r_p, \pi)$ ,  $w_p(r_p)$  and the best fit with a power-law  $\xi(r)$ . This is a fairly conservative selection, reducing each of the three subsamples by  $\sim 30\%$  in number (to 882, 740 and 503 galaxies respectively). For these three samples, we obtain the following estimates for  $(r_0, \gamma)$ :  $(5.95^{+0.34}_{-0.30} h^{-1} \text{ Mpc}, 1.92^{+0.06}_{-0.07})$ ,  $(6.85^{+0.40}_{-0.41} h^{-1} \text{ Mpc}, 1.90^{+0.11}_{-0.06})$ , and  $(7.45^{+0.64}_{-0.64} h^{-1} \text{ Mpc}, 1.74^{+0.11}_{-0.10})$ , respectively. Comparison of these values with those in Table 2 shows that the results are very robust and that our conclusions are unaffected by any magnitude bias affecting the faint end of the Zwicky catalogue.

Figure 9 shows one of our principal results, the relative clustering strength of early- and late-type galaxies, as described by the real-space correlation function. Both the slope and correlation length are significantly different in the two samples (Table 2).

The scale dependence of the relative bias  $b_{ES}$  of early to late-type galaxies is then simply:

$$b_{ES}(r) = \left( \frac{\xi_E(r)}{\xi_S(r)} \right)^{\frac{1}{2}} = b_1 \cdot r^{-\nu} \quad , \quad (7)$$

where  $b_1$  is the value at  $1 h^{-1} \text{ Mpc}$  and  $\nu = (\gamma_S - \gamma_E)^{0.5}$ . We find  $b_{ES}(r) = (2.0 \pm 0.4)r^{-0.16 \pm 0.08}$ , where the error bars have been computed using standard error propagation. At  $r = 5 h^{-1} \text{ Mpc}$ , we find  $b_{ES} = 1.6 \pm 0.4$ . Hermit *et al.* (1996) compute a similar relative bias factor from the Optical Redshift Survey (Santiago *et al.* 1995), but in redshift space, finding an average value  $\sim 1.5$  between 1 and  $10 h^{-1} \text{ Mpc}$ . Their analysis does not take into account the differences in redshift-space distortions between the two classes of galaxies that we have stressed here. Loveday *et al.* (1995) use both the APM catalogue and the sparsely-sampled subsets of galaxies that

---

<sup>8</sup>Note also, however, that  $w_p(r_p)$  is an integral over  $\xi(r)$ , and therefore small deviations from the power-law model in the latter function are averaged out in the former.

form the APM–Stromlo redshift survey; inverting the angular correlation function  $w(\theta)$  for two subsamples limited to  $b_J = 16.57$  they find  $r_0 = 7.76 \pm 0.35 h^{-1}$  Mpc,  $\gamma = 1.87 \pm 0.07$  for early-type galaxies and  $r_0 = 4.49 \pm 0.13 h^{-1}$  Mpc,  $\gamma = 1.72 \pm 0.05$  for late-type galaxies. This is in good agreement with our direct estimates from the spatial function. However, the APM–Stromlo data are too sparse for being able to compute  $\xi(r_p, \pi)$  directly from the morphological subsamples, so that an estimate of the pairwise velocity dispersion  $\sigma_{12}(r)$  cannot be obtained.

The correlation length we find for all spiral galaxies is significantly larger than that of *IRAS* galaxies in the 1.2 Jy redshift survey,  $r_0(1.2 \text{ Jy}) = 3.76^{+0.20}_{-0.23} h^{-1}$  Mpc, while the slope  $\gamma(1.2 \text{ Jy}) = 1.66^{+0.12}_{-0.09}$  is similar. This has the interesting implication that the relative bias of spiral galaxies to *IRAS*–selected galaxies is independent of scale, at least below  $10 h^{-1}$  Mpc. Since *IRAS* galaxies tend to be of type Sb and later, we have defined a volume-limited sample to  $M = -19$ , containing 321 galaxies with types between Sb and Irr. In fact, for these we find a lower correlation length,  $r_0 = 4.05^{+0.57}_{-0.75} h^{-1}$  Mpc, and a similar logarithmic slope,  $\gamma = 1.55^{+0.11}_{-0.13}$ , in excellent agreement with *IRAS* galaxies.

### 4.3. The Pairwise Velocity Dispersion

The quantity  $\xi(r_p, \pi)$  can be expressed as an integral over the product of the real-space correlation function  $\xi(r)$ , and the distribution function of the line-of-sight components  $w_3$  of relative velocities for pairs with separation  $r$ ,  $f(w_3|r)$  (F94b). If  $y$  is the component of  $r$  along the line of sight, then  $w_3 = H_0(\pi - y)$  and the integral can be written as (Peebles 1980, F94b)

$$1 + \xi(r_p, \pi) = H_0 \int_{-\infty}^{+\infty} dy \left\{ 1 + \xi \left[ (r_p^2 + y^2)^{\frac{1}{2}} \right] \right\} f [H_0(\pi - y)|r] . \quad (8)$$

This expression gives a *description* of the effect of a peculiar velocity field on  $\xi(r)$ , but does not represent a self-consistent dynamical treatment of the density and velocity fields, which are clearly interdependent (Fisher 1995). We do not have any *a priori* information, therefore, on the functional form of the distribution function  $f$ . Peebles (1976) first showed that an exponential distribution best fits the observed data, a result subsequently confirmed by  $N$ –body models (e.g., Zurek *et al.* 1994). With such a choice, Eq. (8) becomes

$$1 + \xi(r_p, \pi) = H_0 \int_{-\infty}^{+\infty} dy [1 + \xi(r)] \frac{1}{\sqrt{2}\sigma_{12}(r)} \exp \left\{ -\sqrt{2}H_0 \left| \frac{\pi - y \left[ 1 + \frac{v_{12}(r)}{H_0 r} \right]}{\sigma_{12}(r)} \right| \right\} , \quad (9)$$

where  $r^2 = r_p^2 + y^2$ ,  $v_{12}(r)$  is the mean relative velocity of galaxy pairs with separation  $r$ , and  $\sigma_{12}(r)$  is the pairwise one-dimensional velocity dispersion along the line of sight.

F94b show that it is very difficult to model the dependence of  $v_{12}$  on the separation  $r$ . This is made particularly difficult in our case; our sample covers too small a volume to allow a determination of the large-scale streaming from the compression of the contours of  $\xi(r_p, \pi)$  (cf.,

§ 4.1). For this reason, we do not follow F94b in a detailed analysis of the mean streaming, and instead, we limit ourselves to the simple streaming model introduced by DP83, based on the similarity solution of the BBGKY equations:

$$v_{12}(r) = -H_0 r \frac{F}{1 + \left(\frac{r}{r_0}\right)^2} . \quad (10)$$

We wish to fit Eq. (9) to the observed  $\xi(r_p, \pi)$  to constrain  $\sigma_{12}(r)$ . We are interested in particular in  $\sigma_{12}(1)$ , the pairwise velocity dispersion for scales smaller than  $1 h^{-1}$  Mpc, and thus we carry out all fits to the quantity

$$\xi(\pi) = \int_0^1 dr_p \xi(r_p, \pi) \quad , \quad (11)$$

following F94b<sup>9</sup>. In practice, because we have calculated  $\xi(r_p, \pi)$  in  $1 h^{-1}$  Mpc bins,  $\xi(\pi)$  is simply the value of  $\xi(r_p, \pi)$  in the first bin of  $r_p$ . We assume further that  $\sigma_{12}(r)$  is a weak function of separation  $r$  (DP83), so that it can be treated as a single free parameter,  $\sigma_{12}(1)$ . Figure 10 shows the results of two-parameter fits of the model of Eqs. (9) and (10) to  $\xi(\pi)$  for the E–19.5 and S–19.5 subsamples. We use the best-fit values of  $r_0$  and  $\gamma$  from Table 2 appropriate for each subsample; errors and covariances of  $\xi(\pi)$  are calculated consistently, as described in § 3.3. The quantity  $F$  is very poorly constrained by these data (Figure 10): the free-streaming on these small scales is quite small.

We therefore estimate  $\sigma_{12}(1)$  for the two cases  $F = 0$  (free expansion of pairs with the Hubble flow), and  $F = 1$  (stable clustering). This second case is most probably the one closer to a realistic model: Jain (1996) shows that the stable clustering hypothesis ( $F = 1$ ) should be a good approximation at the present epoch for scales of the order of, or smaller than  $0.7 h^{-1}$  Mpc. We thus use the values with  $F = 1$  in our discussion below.

The value of  $\sigma_{12}(1)$  is of order  $800 \text{ km s}^{-1}$  for PP–19 and PP–19.5, but drops below  $500 \text{ km s}^{-1}$  for PP–20, consistent with the more isotropic contours of  $\xi(r_p, \pi)$  for this case (Figure 6). We interpret this as due to the smaller effect rich clusters, and in particular the Perseus cluster, have on the larger volume of PP–20, as we shall see in the next section. Notice the very significant factor of two difference between the  $\sigma_{12}(1)$  for early- and late-type galaxies at  $M_{Zw} = -19.5$ , a dramatic indication of the effect of cluster cores on the determination of  $\sigma_{12}(1)$ . We now turn to a direct demonstration of the sensitivity of  $\sigma_{12}(1)$  to the presence of rich clusters in the sample.

#### 4.4. Stability of $\sigma_{12}$ for Late-Type Galaxies

Marzke *et al.* (1995) have discussed in detail the effect of the contribution of cluster galaxies to the small-scale pairwise velocity dispersion. The pairwise velocity dispersion is a pair-weighted

---

<sup>9</sup>Our definition of  $\xi(\pi)$  differs from that of F94b by an unimportant normalization factor – cf., their Eq. (7).

statistic, and thus it is heavily weighted in regions of high density, i.e., clusters. Because galaxies in clusters have an intrinsically high velocity dispersion, the inclusion or exclusion of clusters can have a dramatic effect on  $\sigma_{12}$ . Marzke *et al.* showed that the estimates of  $\sigma_{12}(r)$  fluctuate from one sample to the other due to the significant variations in the number of clusters even over volumes as large as those of the CfA2 and SSRS2 surveys. Guzzo *et al.* (1996) showed that  $\sigma_{12}(1)$  dropped from  $\sim 800 \text{ km s}^{-1}$  to  $\sim 600 \text{ km s}^{-1}$  in PP–19, after removing the Perseus cluster. Thus the removal of a single dominant cluster can significantly affect the pairwise velocity dispersion.

Here we explore further the stability of  $\sigma_{12}(1)$ , in the case of spiral galaxies. Using spiral–only samples, we are in practice filtering out the high–density non–linear regions that would otherwise get such high weight in  $\sigma_{12}(1)$ . The result of excluding the Perseus cluster from the PP–19.5 sample is visually shown by the changes in  $\xi(r_p, \pi)$  in the two top panels of Figure 11. The differences between the contours in the two panels [and the corresponding values of  $\sigma_{12}(1)$ , reported in Table 3], can be compared to those produced by the same operation on the S–19.5 sample (bottom). While the effect on PP–19.5 is relevant [although less dramatic than it was found for PP–19 by Guzzo *et al.* (1996) for PP–19, due to the larger volume and the consequent reduced weight of the Perseus cluster], the two bottom panels of Figure 11 are virtually identical, and so are the estimated  $\sigma_{12}(1)$ .

Table 3 also gives  $\sigma_{12}(1)$  for spiral samples limited to  $M_{Zw} = -19$  and  $-20$ . Table 3 indicates that  $\sigma_{12}(1)$  for spirals lies consistently between 300 and 350  $\text{km s}^{-1}$ . This agrees with the F94b value for *IRAS* galaxies  $317^{+40}_{-49} \text{ km s}^{-1}$ , the Marzke *et al.* 1995 value for galaxies outside of  $R \geq 1$  Abell clusters  $295 \pm 99 \text{ km s}^{-1}$ , and the original determination by DP83, which undersampled the Virgo cluster in CfA1 (Somerville, Davis & Primack 1997).

It is interesting to discuss the similarity of  $\sigma_{12}(1)$  for spiral and *IRAS* galaxies, in the light of their different correlation lengths ( $r_0 \simeq 5.5 h^{-1} \text{ Mpc}$  and  $r_0 \simeq 3.8 h^{-1} \text{ Mpc}$ , respectively). *IRAS* galaxies are mostly late–type spirals, and indeed we showed above that if we compute  $\xi(r)$  for this subclass, we recover  $r_0 \simeq 4.0 h^{-1} \text{ Mpc}$ , in agreement with *IRAS* galaxies (cf., Giovanelli, Haynes & Chincarini 1986, and Iovino *et al.* 1993, who showed that there is a continuity in the clustering strength within the spiral class, with Sc’s being less clustered than Sa’s). The similar value of  $\sigma_{12}(1)$ , on the other hand, may simply indicate that the dynamics of *IRAS* galaxies and all spirals are governed by the same fluctuations in the underlying matter density field. Indeed,  $\sigma_{12}(1)$  for galaxies of type Sb and later is found to be  $255^{+105}_{-75} \text{ km s}^{-1}$ , in statistical agreement with the spiral sample as a whole.

## 5. SUMMARY AND DISCUSSION

The main conclusions we have reached in this paper can be summarized as follows.

- We see very strong small–scale redshift–space distortions in the Perseus–Pisces redshift

survey. The distortions are much stronger for early-type galaxies, as one would expect from the segregation of morphological types.

- We confirm a mild luminosity dependence of clustering for absolute magnitudes around the knee of the luminosity function,  $M_{Zw} \sim -19.5$ : the correlation length increases from  $5.95_{-0.31}^{+0.27} h^{-1}$  Mpc for  $M_{Zw} \leq -19$  to  $7.05_{-0.59}^{+0.47} h^{-1}$  Mpc for  $M \leq -20$ . These values are somewhat higher than the “canonical” value of the correlation length based on the DP83 analysis of the CfA1 survey,  $r_0 = 5.4 h^{-1}$  Mpc. This latter value is confirmed by the analysis of the ESO Slice Project (ESP) survey (Bartlett *et al.* 1997), that yields  $r_0 = 4.5_{-0.17}^{+0.15} h^{-1}$  Mpc, while the Las Campanas survey (Lin 1995), gives  $r_0 = 5.00 \pm 0.14 h^{-1}$  Mpc. There are probably two reasons for the higher values of  $r_0$  measured here. First, the “standard” values quoted above are estimates of  $\xi(r)$  performed on apparent-magnitude-limited samples. If there is, as we have seen, a mild luminosity dependence of clustering, samples that are volume-limited at relatively bright absolute magnitudes will systematically measure a higher clustering signal. Second, the Perseus-Pisces area is rather rich in clusters of galaxies, so that it probably over-emphasizes the cluster contribution to  $\xi(r)$ . For comparison, the richest cluster in the CfA1 volume is the Virgo cluster. The CfA2+SSRS2 sample (Marzke *et al.* 1995) covers part of the PP area and thus has a higher contribution of clusters, resulting in  $r_0 = 5.97 \pm 0.15 h^{-1}$  Mpc.
- A meaningful comparison of the relative clustering strength of spirals and ellipticals can be performed only in real space, i.e. after correcting for the effect of differential redshift space distortions. A power-law shape,  $\xi(r) = (r/r_0)^{-\gamma}$ , is a good representation of the real-space correlation function between 1 and  $10 h^{-1}$  Mpc for both ellipticals and spirals. Our best-fit estimate of the power-law parameters gives  $r_0 = 8.35_{-0.76}^{+0.75} h^{-1}$  Mpc,  $\gamma = 2.05_{-0.08}^{+0.10}$  for ellipticals, and  $r_0 = 5.55_{-0.45}^{+0.40} h^{-1}$  Mpc,  $\gamma = 1.73_{-0.08}^{+0.07}$  for spirals. We model the relative bias of the two types of galaxies as a power law with a mild dependence on scale,  $b_{ES}(r) = (2.0 \pm 0.4) (r/1 h^{-1} \text{ Mpc})^{-0.16 \pm 0.08}$ . Furthermore, we confirm the continuous variation of clustering strength also within the spiral class. For late-type spirals (Sb and later), and irregulars, we estimate  $r_0 = 4.05_{-0.75}^{+0.57} h^{-1}$  Mpc, and  $\gamma = 1.55_{-0.13}^{+0.11}$ , virtually the same correlation function as *IRAS* galaxies.
- The quantity  $\sigma_{12}(1)$ , the measured pairwise velocity dispersion between 0 and  $1 h^{-1}$  Mpc, varies considerably between samples of different volumes, going from  $855_{-75}^{+85} \text{ km s}^{-1}$  of PP-19, to  $465_{-105}^{+145} \text{ km s}^{-1}$  for PP-20. This variation is consistent with the smallness of the volume sampled.
- The difference in the measured  $\sigma_{12}(1)$  between early- and late-type galaxies is remarkable. We estimate  $\sigma_{12}(1) = 865_{-165}^{+250} \text{ km s}^{-1}$  for ellipticals and  $\sigma_{12}(1) = 345_{-65}^{+95} \text{ km s}^{-1}$  for spirals. Contrary to results for the combined sample, the value of  $\sigma_{12}(1)$  for spiral galaxies alone is stable to both changes in the sample volume and the presence of rich clusters. The consistency of this value with those measured for non-cluster galaxies (Marzke *et al.* 1995)

and *IRAS* galaxies (F94b), and the stability among spiral subclasses (for Sb and later types we measure  $255_{-75}^{+105}$  km s<sup>-1</sup>), suggests that a value  $\sigma_{12}(1)$  in the range 300 – 350 km s<sup>-1</sup> is a good estimate of the “temperature” of the galaxy flow outside of virialized structures.

LG gratefully thanks J.P. Ostriker for hospitality at Princeton University, where part of this work was done, and J. Bartlett, M. Davis and P.J.E. Peebles for fruitful discussions. We thank the referee, Ron Marzke, for his valuable comments and suggestions. MAS acknowledges the generous support of the Alfred P. Sloan Foundation. This work was partly supported by grants AST90–23450 and AST95–28860 to MPH and AST94–20505 to RG.

## REFERENCES

- Bartlett, J.G., Guzzo, L., Vettolani, P., Zucca, E., Cappi, A., *et al.* 1997, *A&A*, to be submitted
- Bothun, G.D., & Cornell, M.E. 1990, *AJ*, 99, 1004
- Burstein, D., & Heiles, C. 1978, *ApJ*, 225, 40
- Davis, M., & Geller, M. J. 1976, *ApJ*, 208, 13
- Davis M. & Peebles, P.J.E. 1983, *ApJ*, 267, 465 (DP83)
- Dressler, A. 1980, *ApJ*, 236, 351
- Eisenstein, D.J., Loeb, A., & Turner, E.L. 1997, *ApJ*, 475, 421
- Fisher, K.B. 1995, *ApJ*, 448, 494
- Fisher, K.B., Davis, M., Strauss, M.A., Yahil, A., & Huchra, J.P. 1994a, *MNRAS*, 266, 50 (F94a)
- Fisher, K.B., Davis, M., Strauss, M.A., Yahil, A., & Huchra, J.P. 1994b, *MNRAS*, 267, 927 (F94b)
- Giovanelli, R., & Haynes, M.P. 1991, *ARA&A*, 29, 499
- Giovanelli, R., Haynes, M.P., and Chincarini, G.L. 1986, *ApJ*, 300, 77
- Giovanelli, R., Haynes, M.P., Wegner, G., da Costa, L., Freudling, W. and Salzer, J. 1996, *ApJ*, 464, L99
- Guzzo, L., Fisher, K.B., Strauss, M.A., Giovanelli, R., and Haynes, M.P. 1996, *Astroph. Lett. & Comm.*, 33, 231
- Hamilton, A.J.S. 1988, *ApJ*, 332, 67
- Hamilton, A.J.S. 1993, *ApJ*, 417, 19

- Hermit, S., Lahav, O., Santiago, B.X., Strauss, M.A., Davis, M., Dressler, A., & Huchra, J.P. 1996, MNRAS, 283, 709
- Huchra, J. P., Davis, M., Latham, D., & Tonry, J. 1983, ApJS, 52, 89
- Iovino, A., Giovanelli, R., Haynes, M.P., Chincarini, G., & Guzzo, L. 1993, MNRAS, 265, 21
- Iovino, A., Warren, S.J., Shaver, P.A., & Hewett, P. 1996, *Astroph. Lett. & Comm.*, 33, 143
- Jain, B. 1996, preprint (astro-ph/9605192)
- Lin, H. 1995, Ph.D. Thesis, Harvard University
- Ling, E. N., Frenk, C. S., & Barrow, J. D. 1986, MNRAS, 223, 21P
- Loveday, J., Maddox, S.J., Efstathiou, G., & Peterson, B.A., 1995, ApJ, 442, 457
- Marzke, R.O., Geller, M.J., da Costa, L.N., & Huchra, J.P., 1995, AJ, 110, 477
- Mo, H.J., Jing, Y.P., & Börner, G. 1993, MNRAS, 264, 82
- Peebles, P.J.E. 1976, Ap&SS, 45, 3
- Peebles P.J.E. 1980, *The Large-Scale Structure of the Universe* (Princeton: Princeton University Press)
- Postman, M., & Geller, M. J. 1984, ApJ, 281, 95
- Santiago, B. X., Strauss, M. A., Lahav, O., Davis, M., Dressler, A., & Huchra, J. P. 1995, ApJ, 446, 457
- Somerville, R.S., Davis, M., and Primack, J.R. 1997, ApJ, 479, 616
- Strauss, M. A., Davis, M., Yahil, A., & Huchra, J. P. 1992, ApJ, 385, 421
- Willick, J.A. 1990, ApJ, 351, L5
- Zurek, W., Quinn, P.J., Warren, M.S., & Salmon, J.K. 1994, ApJ, 431, 559
- Zwicky, F., Herzog, E., Wild, P., Karpowicz, M., & Kowal, C. 1961-68, *Catalogue of Galaxies and of Clusters of Galaxies*, (Pasadena: California Institute of Technology)

Sample	$\sigma_{12}(1) (F=0)$	$\sigma_{12}(1) (F=1)$
PP-19	$775^{+85}_{-65}$	$855^{+85}_{-75}$
PP-19.5	$735^{+155}_{-115}$	$805^{+155}_{-115}$
PP-19.5-NOP	$625^{+125}_{-85}$	$725^{+135}_{-95}$
PP-20	$525^{+155}_{-115}$	$465^{+145}_{-105}$
S-19	$205^{+75}_{-55}$	$295^{+75}_{-55}$
S-19.5	$255^{+95}_{-65}$	$345^{+95}_{-65}$
S-19.5-NOP	$235^{+115}_{-75}$	$325^{+125}_{-85}$
S-20	$415^{+465}_{-245}$	$485^{+465}_{-245}$
E-19.5	$815^{+245}_{-165}$	$865^{+250}_{-165}$

Table 3: Summary of the best estimates of the pairwise velocity dispersion between 0 and 1  $\text{h}^{-1}$  Mpc,  $\sigma_{12}(1)$ , for the two cases  $F = 0$  (free streaming with the Hubble flow), and  $F = 1$  (stable clustering). All estimates are in  $\text{km sec}^{-1}$ .

Fig. 1.— The distribution on the sky of all galaxies with  $M_{Zwicky} \leq 15.5$  after correction for extinction. The upper solid line marks the border of the high-extinction region excluded from the sample. The large lump of objects near  $\alpha \sim 3.2^h$ ,  $\delta \sim 41^\circ$  is the Perseus cluster.

Fig. 2.— Galaxy distribution in the volume-limited samples to  $M_{Zw} = -19.5$  and  $M_{Zw} = -20$ , including all morphological types.

Fig. 3.— The spatial distribution of early-type and late-type galaxies, volume-limited to  $M_{Zw} = -19.5$ .

Fig. 4.— Histograms of the redshift distribution in four representative volume-limited samples. Top panels: all galaxies. Bottom panels: early-type and late-type galaxies separately. The dashed lines are the distributions expected in the absence of structure.

Fig. 5.—  $\xi(r_p, \pi)$  for PP-19. In this and the following  $\xi(r_p, \pi)$  maps, the heavy contour corresponds to  $\xi = 1$ ; for larger values of  $\xi$ , contours are logarithmically spaced, with  $\Delta \log_{10} \xi = 0.1$ ; below  $\xi = 1$ , they are linearly spaced with  $\Delta \xi = 0.2$  down to  $\xi = 0$ . The dashed contours represent the isotropic correlations expected in the absence of peculiar velocities. The right-hand panel has been Gaussian-smoothed with an isotropic filter of width  $3 h^{-1}$  Mpc.

Fig. 6.—  $\xi(r_p, \pi)$  for PP-19.5 and PP-20, Gaussian smoothed.

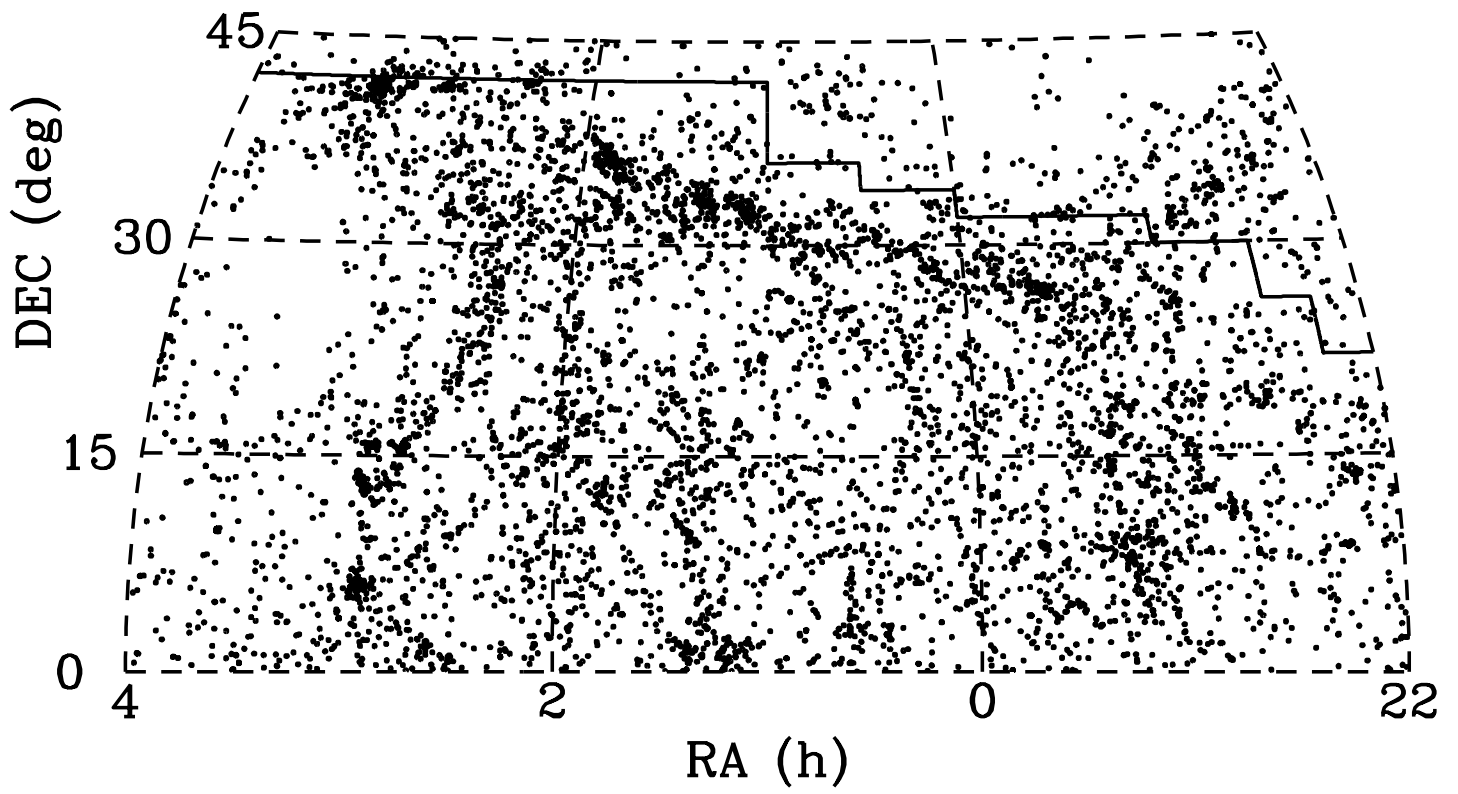
Fig. 7.—  $\xi(r_p, \pi)$  for the early-type and late-type samples, E-19.5 and S-19.5, respectively, Gaussian-smoothed.

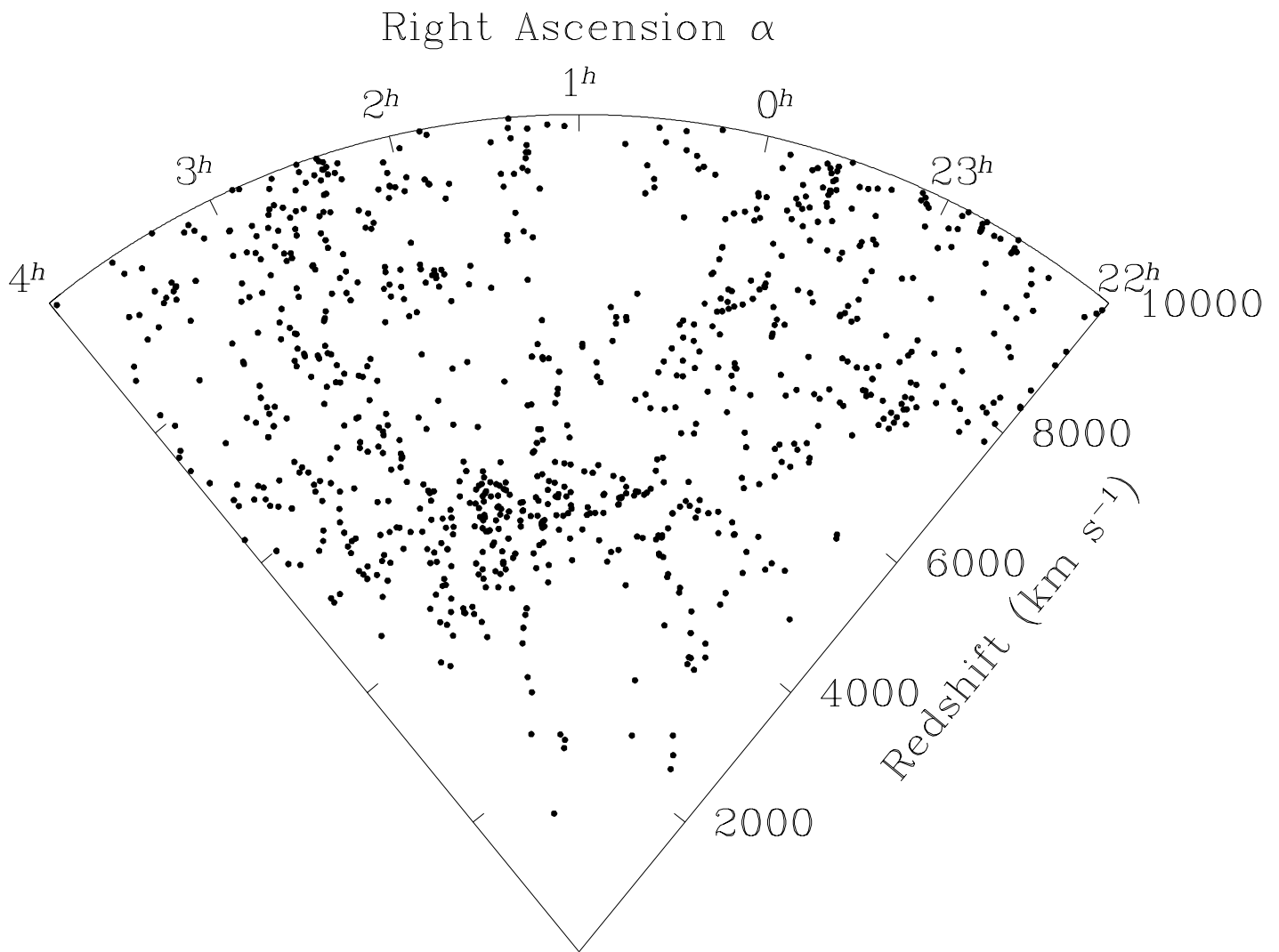
Fig. 8.— The projected correlation function  $w_p(r_p)$  and results of fits of the power-law model, for the three volume-limited samples. The error bars are given by bootstrap resampling. The contours give the 68.3%, 95.4% and 99.73% confidence levels on the two parameters taken separately.

Fig. 9.— As in Figure 8, for early- and late-type galaxies, separately. Note the very significant separation in parameter space between the two classes.

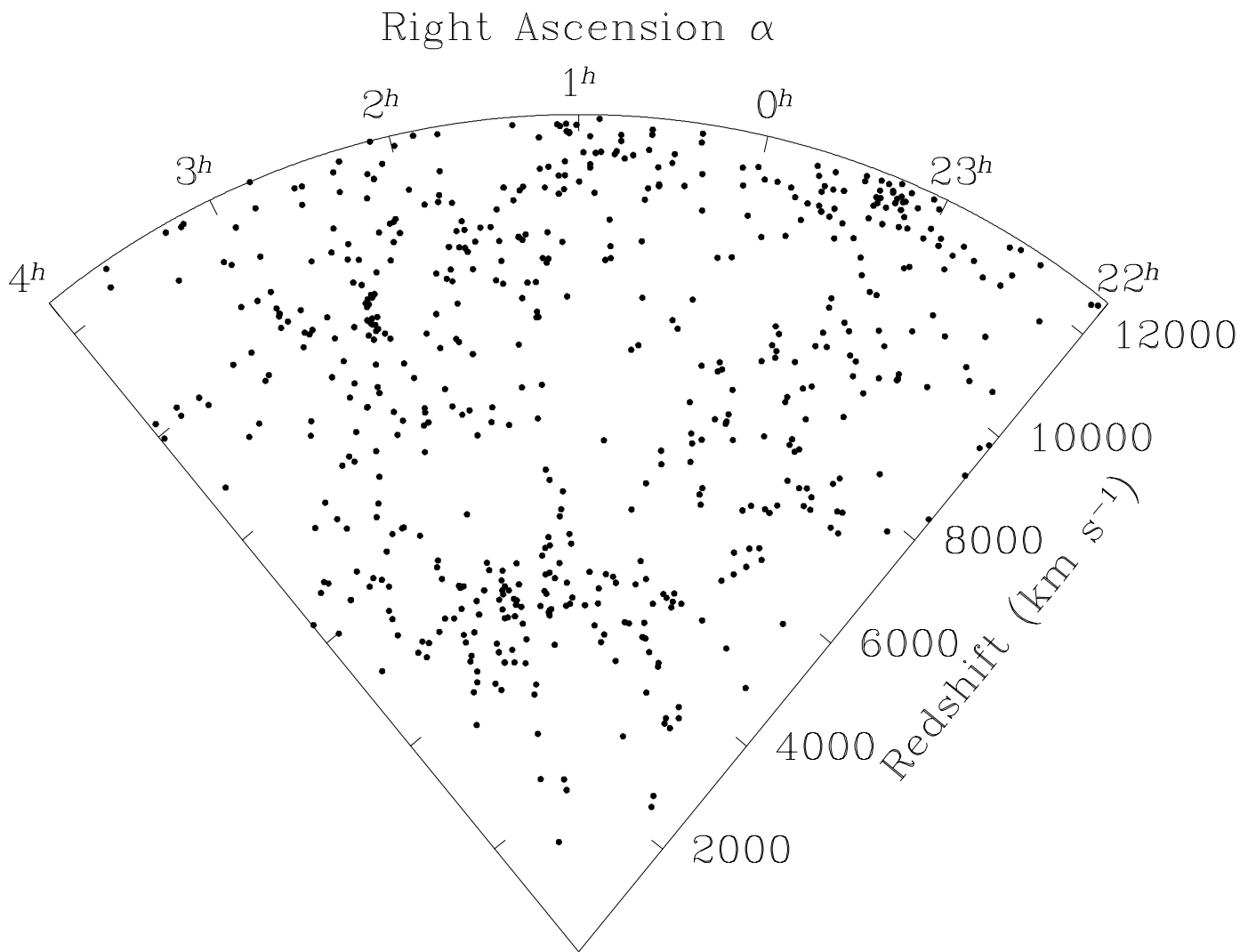
Fig. 10.— Example of full two-parameter fits to  $\xi(r_p, \pi)$  based on the model of Eq. (9), to show how poorly constrained the streaming amplitude  $F$  is. Contour levels are as in Figure 8.

Fig. 11.— The effect on  $\xi(r_p, \pi)$  of removing the largest “Finger of God” from the sample. Right panels show the effect of excluding the high-velocity-dispersion Perseus cluster. Top panels are for PP-19.5, bottom for S-19.5. Note the change between the two top panels, while for spirals the removal of the cluster has very little effect on the measured  $\xi(r_p, \pi)$ .

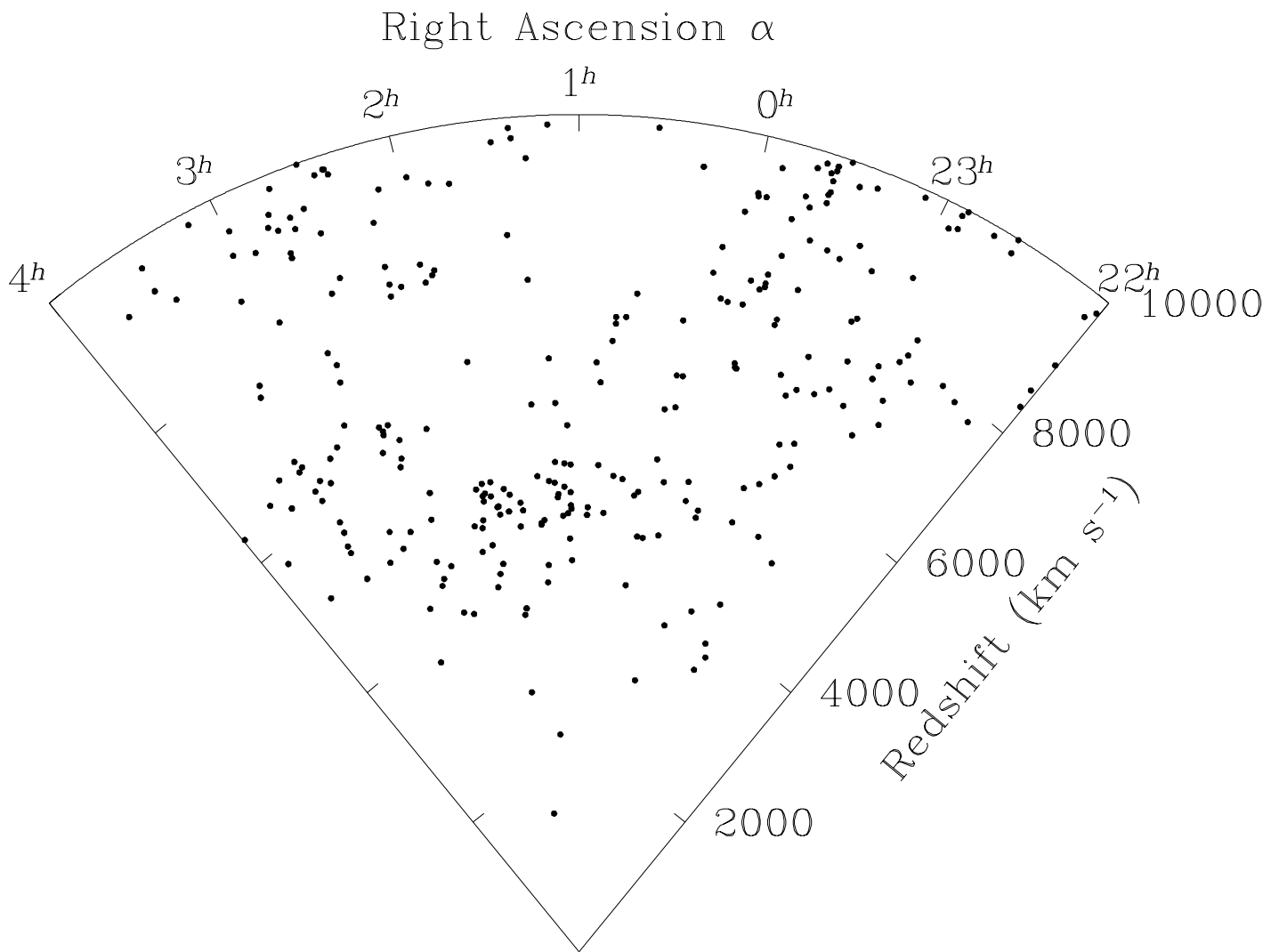




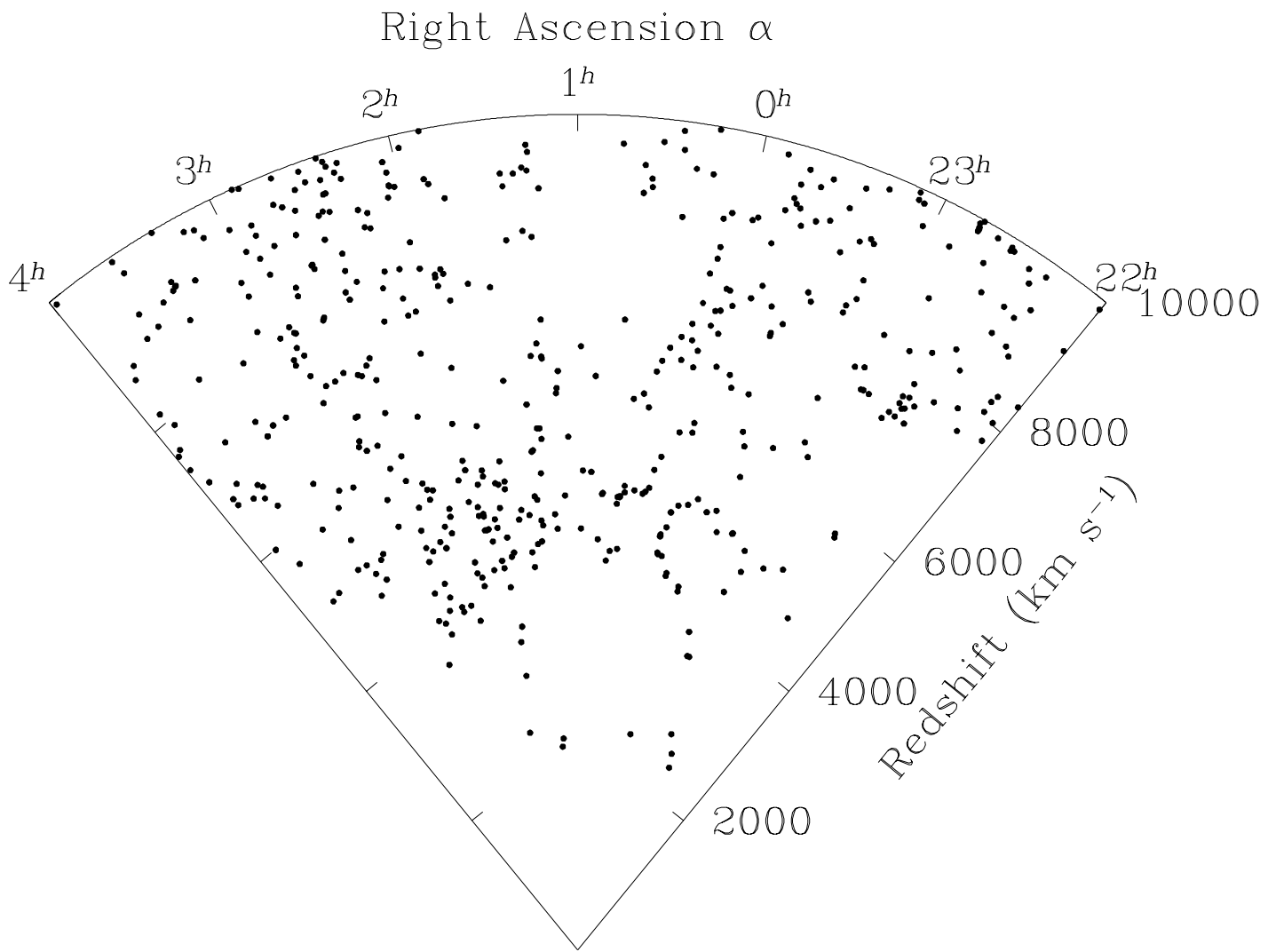
$0^\circ < \delta < 42^\circ$



$$0^\circ < \delta < 42^\circ$$



$0^\circ < \delta < 42^\circ$



$0^\circ < \delta < 42^\circ$

